Draft version September 23, 2021
Typeset using LaTeX **twocolumn** style in AASTeX63

arXiv:2009.00579v2 [astro-ph.HE] 1 Dec 2020

GRB 160625B: Evidence for a Gaussian-Shaped Jet

Virginia Cunningham,[1,2] S. Bradley Cenko,[3,4] Geoffrey Ryan,[4] Stuart N. Vogel,[1] Alessandra Corsi,[5] Antonino Cucchiara,[6] Andrew S. Fruchter,[7] Assaf Horesh,[8] Tuomas Kangas,[7] Daniel Kocevski,[9] Daniel A. Perley,[10] and Judith Racusin[3]

[1] *Department of Astronomy, University of Maryland, College Park, MD 20742, USA*
[2] *Center for Research and Exploration in Space Science and Technology, NASA/GSFC, Greenbelt, MD 20771*
[3] *Astrophysics Science Division, NASA Goddard Space Flight Center, MC 661, Greenbelt, MD 20771, USA*
[4] *Joint Space-Science Institute, University of Maryland, College Park, MD 20742, USA*
[5] *Department of Physics and Astronomy, Texas Tech University, Box 1051, Lubbock, TX 79409-1051, USA*
[6] *College of Marin/University of the Virgin Islands, 120 Kent Ave., Kentfield, CA 94904, USA*
[7] *Space Telescope Science Institute, 3700 San Martin Drive, Baltimore, MD 21218, USA*
[8] *Racah Institute of Physics, The Hebrew University of Jerusalem, Jerusalem, 91904, Israel*
[9] *Astrophysics Office, ST12, NASA/Marshall Space Flight Center, Huntsville, AL 35812, USA*
[10] *Astrophysics Research Institute, Liverpool John Moores University, Liverpool Science Park, 146 Brownlow Hill, Liverpool L35RF, UK*

(Received August 25, 2020; Revised October 16, 2020; Accepted October 18, 2020; Published September 23, 2021)

Submitted to ApJ

ABSTRACT

We present multiwavelength modeling of the afterglow from the long γ-ray burst GRB 160625B using Markov Chain Monte Carlo (MCMC) techniques of the `afterglowpy` Python package. GRB 160625B is an extremely bright burst with a rich set of observations spanning from radio to γ-ray frequencies. These observations range from $\sim$0.1 days to >1000 days, thus making this event extremely well-suited to such modeling. In this work we compare top-hat and Gaussian jet structure types in order to find best fit values for the GRB jet collimation angle, viewing angle, and other physical parameters. We find that a Gaussian-shaped jet is preferred (2.7-5.3σ) over the traditional top-hat model. Our estimate for the opening angle of the burst ranges from 1.26° to 3.90°, depending on jet shape model. We also discuss the implications that assumptions on jet shape, viewing angle, and particularly the participation fraction of electrons have on the final estimation of GRB intrinsic energy release and the resulting energy budget of the relativistic outflow. Most notably, allowing the participation fraction to vary results in an estimated total relativistic energy of $\sim 10^{53}$ erg. This is two orders of magnitude higher than when the total fraction is assumed to be unity, thus this parameter has strong relevance for placing constraints on long GRB central engines, details of the circumburst media, and host environment.

1. INTRODUCTION

Long γ-ray bursts (GRBs)[1] are amongst the most violent and energetic phenomena in the Universe. Despite observations of thousands of GRBs over the last few decades, key open questions – such as the nature of the central engine and the structure and composition of the relativistic jets – remain unsolved.

Corresponding author: Virginia Cunningham
vcunning@astro.umd.edu

[1] The primary focus throughout this paper will be on long-duration GRBs, unless otherwise noted.

One key to unraveling these mysteries lies in accurately measuring their energetics. Estimates of the total relativistic energy released by a GRB can have major implications for constraining their physical characteristics and origins. Precise measurements could potentially distinguish between different progenitor systems. Two popular theories include rotationally-powered magnetars (Zhang & Mészáros 2001; Thompson et al. 2004; Metzger et al. 2015) and the collapse of a massive star into a black hole (Woosley 1993; MacFadyen & Woosley 1999; Woosley & Heger 2012).

GRBs are known to be highly collimated explosions with jet opening angles typically between 1–10° (Sari et al. 1999; Rhoads 1999). The true value of the in-

trinsic energy release of a GRB is dependent upon this collimation angle: $E_\gamma = E_{\gamma,\rm iso}(1-\cos\theta_j) \approx E_{\gamma,\rm iso}\frac{\theta_j^2}{2}$, where E_γ is the beaming-corrected γ-ray energy of the burst, $E_{\gamma,\rm iso}$ is the uncorrected isotropic γ-ray energy, and θ_j is the jet half-opening angle[2] (Bloom et al. 2001; Frail et al. 2001). This jet collimation correction can affect the value of E_γ by a factor of 10 – 100 (Frail et al. 2001). Therefore a precise measurement of θ_j is imperative for understanding the true energetics of GRBs.

Making a precise measurement of the collimation angle can be difficult however, as it usually requires sustained, detailed, multiwavelength observations of the GRB afterglow and the identification of a 'jet-break', i.e., a change in the temporal slope of the light curve associated with the observer becoming aware of the edge of the jet (Sari et al. 1999; Panaitescu 2007; Kocevski & Butler 2008; Racusin et al. 2009; Goldstein et al. 2016). Alternatively, the energy of the explosion can be inferred via non-relativistic calorimetry (Frail et al. 2000; Berger et al. 2004). At late times the ejecta slows to a non-relativistic spherical blastwave and can be modeled independently of the jet collimation angle. This is of course only possible when sufficiently late-time radio data exists.

Here we focus on events detected at GeV energies by the Large Area Telescope (LAT; Atwood et al. 2009) on *Fermi*. This sample is well-suited for studying GRB energetics since *Fermi* tends to select events with high values of $E_{\gamma,\rm iso}$. This effect can be partly explained by both the Amati Relation ($E_{peak} - E_{\gamma,\rm iso}$, Amati et al. 2009) and also the lower sensitivity of the LAT compared to X-ray instruments. LAT-detected GRBs often display values of $E_{\gamma,\rm iso} > 10^{53}$ erg (Figure 1; Cenko et al. 2010, 2011; Xu et al. 2013; Perley et al. 2014) and their afterglows can generally be well modeled by a series of more simple power laws (Yamazaki et al. 2019).

We are conducting a campaign to model the broadband behavior of a sample of LAT-detected GRBs. Here we present the methodology and apply this to one example, that of GRB 160625B - an exceptionally bright long-GRB at z=1.406 (Xu et al. 2016). Future work will discuss the broader population in the hopes of identifying whether LAT GRBs in fact represent a unique group and if so, how they differ from the rest of the GRB population (e.g., jet shape, local environments, magnetar vs black hole central engines; Racusin et al. 2011).

Several previous works have already performed detailed afterglow analysis of GRB 160625B (Troja et al. 2017; Alexander et al. 2017; Kangas et al. 2020, hereafter T17, A17 and K20, respectively). We expand on these works by combining and including all available data as well as undertaking new late-time observations with the Very Large Array (VLA). We also expand the analysis by considering additional models for the internal structure of the GRB jet beyond the canonical top-hat model as well as taking into account viewing angle effects, quantifying the uncertainty of derived parameters, and investigating the role individual afterglow parameters, such as the participation fraction, ξ, have on the model fitting.

For our modeling of GRB 160625B, we make use of the new `afterglowpy` software package (Ryan et al. 2020). `Afterglowpy` is a publicly available open-source Python package for the numerical computation of structured jet afterglows. This package is unique in its ability to test a range of jet structures such as top-hat, Gaussian, and power law while leaving the viewing angle and jet collimation angle as free parameters. There is evidence to suggest that the interaction between the GRB jet and the surrounding medium could take on a variety of forms - based on numerical simulations (Aloy et al. 2005; Duffell & MacFadyen 2013a; Margutti et al. 2018) and observations of GW 1701817/GRB 170817A (Lazzati et al. 2018; Troja et al. 2018). In fact, most GRB jets probably deviate significantly from the simple on-axis top-hat model (e.g., Ryan et al. 2015) and Strausbaugh et al. (2019) has already suggested GRB 160625B can be modeled as a structured jet so it is imperative to consider this when modeling GRB afterglows.

This paper is organized as follows: we describe the available data products and our data reduction methods in §2. In §3 we define the details of the GRB afterglow modeling. We discuss the implications of our results in §4 and summarize our conclusions in §5. All error bars correspond to 1σ uncertainties and we assume a standard ΛCDM cosmology (Planck Collaboration et al. 2018) throughout the analysis.

2. OBSERVATIONS AND DATA REDUCTION

2.1. γ-ray

The *Fermi* Gamma-ray Burst Monitor (GBM; Meegan et al. 2009) first triggered on GRB 160625B at 22:40:16.28 UT on 25 June 2016 (UT times are used throughout this work) and again at 22:51:16.03. The burst is characterized by three 'sub pulses' separated by two relatively quiescent periods over a duration of t_{90} = 460s (50-300 keV) and the spectral shape of the burst is well modeled by a Band function (Burns 2016). The fluence in the 10-1000 keV bandpass was

[2] This equation is only valid for the simple top-hat jet. More complicated jet structure types are discussed in §3.2.2

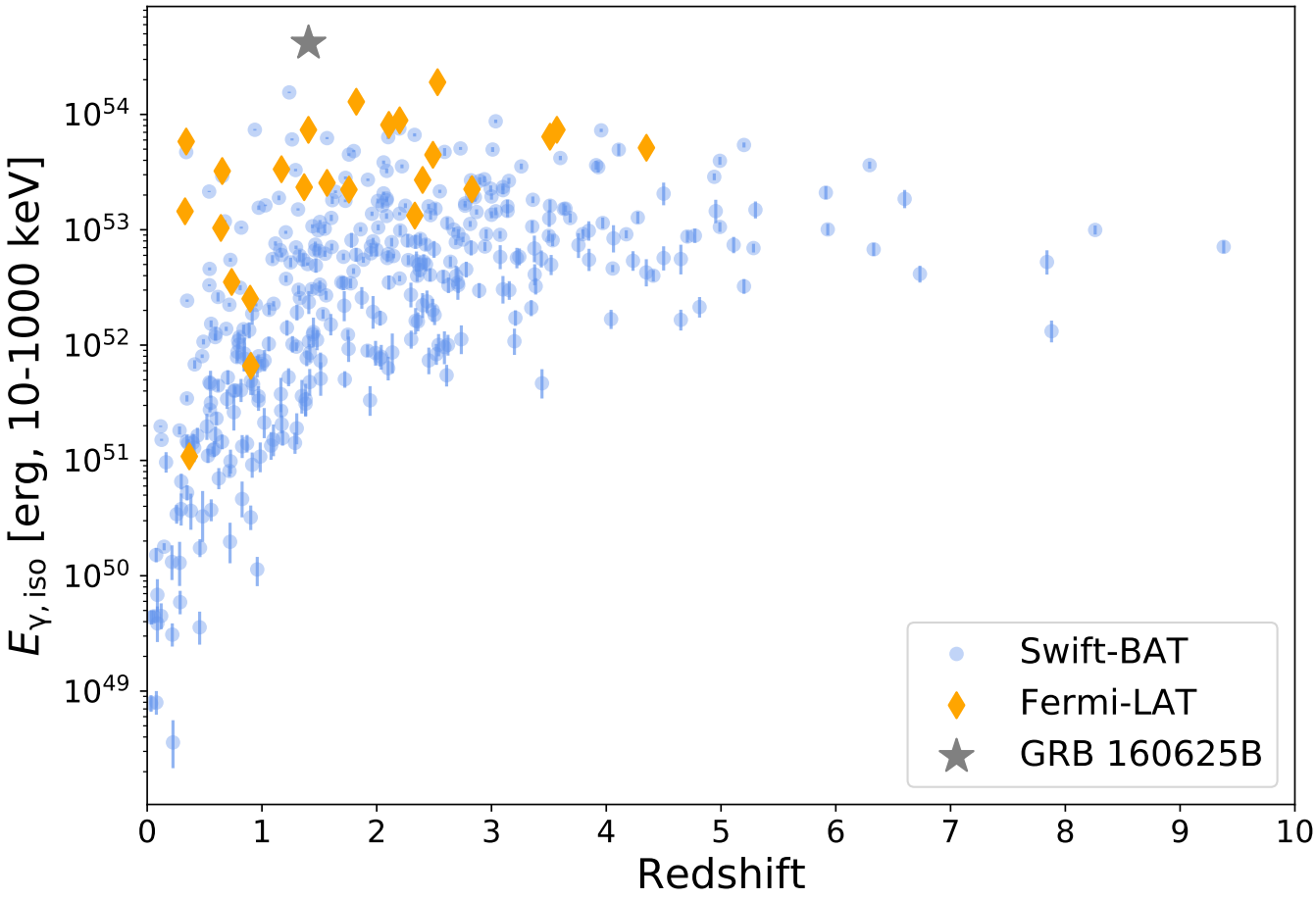


Figure 1. Bolometric (10-1000 keV) isotropic energy release vs redshift compared between LAT-detected and BAT-detected GRBs. In general, GRBs detected by LAT tend to be brighter, more energetic events and GRB 160625B is itself extreme even for this population. Data are taken from Lien et al. (2016) and Ajello et al. (2019).

$(6.4256 \pm 0.0019) \times 10^{-4}$ erg cm^{-2} (von Kienlin et al. 2020).

The *Fermi* Large Area Telescope (LAT; Atwood et al. 2009) triggered on the second pulse at 22:43:24.82. The GRB location was in the LAT field-of-view for ∼1000 seconds after its initial trigger (20 MeV to 300 GeV, Dirirsa et al. 2016). The highest energy photon observed in the rest-frame was 15.3 GeV which occurred ∼345 seconds after the first GBM trigger (Ajello et al. 2019).

The GRB was also detected by Konus-*Wind* ($9.44 \pm 0.16 \times 10^{-4}$ erg cm^2) from 20 keV to 10 MeV, Svinkin et al. 2016), SPI-ACS/INTEGRAL (Kann 2016), and CALET (Nakahira et al. 2016). For the anaylsis presented here we choose t_0 to be that corresponding to the first GBM trigger[3].

[3] Most other analyses reference t_0 to that of the LAT trigger, but since we are ignoring very early data we consider any differences negligible.

2.2. *X-Ray*

The *Neil Gehrels Swift Observatory* (Gehrels et al. 2004) began observing GRB 160625B 2.5 hours after the initial GBM trigger (Evans 2016). The X-ray Telescope (XRT; Burrows et al. 2005) on board *Swift* observed GRB 160625B for 47 days. XRT data are taken from the publicly available online *Swift* burst analyzer tool[4]. For details of how these light curves were produced, see Evans et al. (2007, 2009). The hardness ratio appears relatively constant over time so we assume a single spectrum that can be described as an absorbed power law with the Galactic neutral hydrogen column fixed to 9.76×10^{20} cm^{-2} (Willingale et al. 2013). Using a photon index of $\Gamma_x = 1.86^{+0.10}_{-0.09}$, assuming an intrinsic host absorption of $n_{\mathrm{H,int}} = 1.8 \times 10^{21}$ cm^{-2}, an unabsorbed counts-to-flux conversion factor of 4.4×10^{-11} erg cm^{-2} ct^{-1}, and a redshift of 1.406 (Xu et al. 2016) we convert

[4] https://www.swift.ac.uk/burst_analyser/00020667/

Table 1. X-ray Data

Δt [day]	Energy [keV]	Flux Density [nJy]	Instrument
0.12	5	4787 ± 1076	*Swift*/XRT
0.12	5	4358 ± 981	*Swift*/XRT
0.12	5	5671 ± 1244	*Swift*/XRT
0.12	5	4772 ± 1073	*Swift*/XRT
...	...	...	...
41.31	5	1.34 ± 0.38	*Swift*/XRT
47.16	5	1.06 ± 0.47	*Swift*/XRT
69.76	5	0.61 ± 0.12	*Chandra*/ACIS-S
144.36	5	0.13 ± 0.03	*Chandra*/ACIS-S

1. Times are in reference to the first GBM trigger (Jun 25 2016 22:40:16.28 UTC).
2. This table is available in its entirety in a machine-readable format. A portion is shown here for guidance regarding its form and content.

the 0.3-10 keV flux light curves to a flux density at an energy of 5 keV. We choose only to include data taken during photon counting mode, which begins 0.1 days after the burst. In addition to the XRT data we include the late-time *Chandra* observations taken by K20 at 69.8 and 144 days after the burst. All X-ray observations are available in Table 1.

2.3. *Optical*

One defining feature of GRB 160625B is its extremely bright optical afterglow and the presence of an optical 'bump' around the time of the jet-break. Strausbaugh et al. (2019) suggest this excess emission could be the result of an edge-brightened jet while K20 suggest it could instead be produced by density fluctuations within the circumburst medium or angular brightness differences.

A17 utilized several optical instruments to observe the GRB – the 2 m Faulkes Telescope North (FTN) operated by Las Cumbres Observatory (LCO), the 2 m Liverpool Telescope (LT) at Roque de los Muchachos Observatory (ORM), and the Low Dispersion Survey Spectrograph 3 (LDSS3) at Magellan – ranging from 0.56 to 37 days post trigger. T17 observed the GRB with the Reionization And Transients InfraRed camera (RATIR) beginning 8 hours after the trigger until it faded beyond detection at ∼50 days and also reported u-band observations taken with the Ultraviolet/Optical Telescope (UVOT; Roming et al. 2005) on board *Swift*. In addition, several observations used in this work were compiled from the Gamma-ray Burst Coordinates Network (GCN) Circulars by Zhang et al. (2018) and appropriately converted to flux densities. Late time Hubble Space Telescope (HST) observations were reported by K20 71.5 and 140.2 days post trigger. The flux contribution from the host was already subtracted out by K20 and we account for Galactic extinction in the direction of the GRB, E(B-V) = 0.1107 mag (Schlafly & Finkbeiner 2011), by assuming the extinction law described in Fitzpatrick (1999). All optical observations are available in Table 2.

2.4. *Radio*

We consolidate previous Karl G. Jansky VLA observations (Program IDs 15A-235 and S81171, PIs Berger and Cenko, respectively) from 1.37 to 209 days after the burst for the most complete sample of radio data (A17, K20). We obtained additional late time observations of GRB 160625B taken at 6 GHz (C-band) on 4 Feb 2020 15:14:24 (1319 days post-burst; Program ID SC1031, PI Cenko) for an on-source integration time of 1.8 hours. The data were reduced using the standard VLA calibration pipeline provided by the Common Astronomy Software Applications package (CASA; McMullin et al. 2007). We use J2049+1003 as the complex gain calibrator and 3C286 as both the bandpass and flux calibrator. Imaging is done using the TCLEAN algorithm in CASA. We do not detect any emission at the afterglow location and so report a 3σ upper limit of 7.4 μJy. We calculate this limit as three times the RMS uncertainty at the position of the GRB. In addition, we include data from the Australian Telescope Compact Array (ATCA) taken by T17 between 4.5 and 29 days post burst. All radio observations are available in Table 3.

3. AFTERGLOW MODELING

3.1. *Basic Tenets*

The primary focus of this section is to model the broadband afterglow emission of GRB 160625B with the goal of measuring the total energy output of the GRB central engine, the jet opening angle, and the geometry of the jet structure. Here, we assume the standard fireball model for the afterglow where the observed emission is synchrotron radiation from electrons in the circumburst medium accelerated by the relativistic blast wave (Sari et al. 1998; Granot & Sari 2002). The emitting electrons are accelerated to a power-law distribution of energies with an index of $-p$ and a minimum Lorentz factor of γ_m. The resulting spectral energy distribution (SED) can be described by a series of power law segments smoothly broken at three characteristic frequencies – ν_{sa}, the self-absorption frequency, ν_m, the frequency of the lowest energy electron in the distribution, and ν_c, the cooling frequency. The values of the frequencies depend on the structure of the surrounding medium of the explosion as well as the jet shape, jet microphysics, energy produced, and viewing angle.

Table 2. Optical Data

Δt [day]	Filter	AB Mag	Frequency [$\times 10^{14}$ Hz]	Flux Density [μJy]	Instrument
0.37	r	18.24 ± 0.01	4.82	240 ± 2	RATIR
0.39	r	18.29 ± 0.01	4.82	229 ± 2	RATIR
0.41	r	18.35 ± 0.01	4.82	216 ± 2	RATIR
0.43	r	18.43 ± 0.01	4.82	202 ± 2	RATIR
...	...	...	...	...	...
37.92	R	23.68 ± 0.10	4.68	1.57 ± 0.15	SAORAS/BTA
40.29	R	23.52 ± 0.10	4.68	1.82 ± 0.18	Maidanak/AZT-22
44.34	R	23.90 ± 0.11	4.68	1.28 ± 0.14	Maidanak/AZT-22
44.34	R	<23.01	4.68	<2.91	Maidanak/AZT-22

1. Magnitudes are not corrected for extinction, while flux densities are. Times are in reference to the first GBM trigger (Jun 25 2016 22:40:16.28 UTC).
2. This table is available in its entirety in a machine-readable format. A portion is shown here for guidance regarding its form and content.

Table 3. Radio Data

Δt [day]	Frequency [GHz]	Flux Density [μJy]	Instrument
1.37	5.00	163 ± 34	VLA
1.37	7.10	232 ± 22	VLA
1.35	8.50	288 ± 23	VLA
1.35	11.00	507 ± 35	VLA
...	...	...	...
58.25	6.10	75 ± 10	VLA
58.25	22.00	52 ± 12	VLA
208.95	6.10	16 ± 5	VLA
1319	6.10	<2.46	VLA

1. Times are in reference to the first GBM trigger (Jun 25 2016 22:40:16.28 UTC).
2. This table is available in its entirety in a machine-readable format. A portion is shown here for guidance regarding its form and content.

Before calculating detailed models, we infer the circumburst density profile via the temporal decline rate of the observations. From t $\sim$ 0.1 days to t = 20 days the optical and X-ray data can be well approximated by a single power law. Then at around 20 days the decay steepens, signifying the jet-break[5]. For the early time i-band data we find $\alpha_{\rm i} = -1.00 \pm 0.02$ and for the early XRT observations we find $\alpha_{\rm X} = -1.26 \pm 0.02$. The steepening of the slope between the optical and X-ray observations suggests that the cooling frequency, ν_c, lies between these two regimes. In the case of a slow-cooling constant-density (ISM-like) profile $\alpha_{ISM} = \frac{3(1-p)}{4}$ ($\nu < \nu_c$) which yields an estimate for p, the index of the electron energy distribution, of 2.33 ± 0.03 (Granot & Sari 2002). In the slow-cooling wind-like scenario $\alpha_{wind} = \frac{(1-3p)}{4}$ which yields $p = 1.67 \pm 0.03$. When $\nu > \nu_c$ the decline rate can be described by $\alpha = \frac{(2-3p)}{4}$ for both the wind and ISM-like profiles. Using $\alpha_{\rm X} = -1.26 \pm 0.02$ we find $p = 2.35 \pm 0.03$, consistent with the ISM result. Despite fewer observations available at later times (> 20 days) the optical decline rate of $\alpha_{\rm i,late} = -1.61 \pm 0.16$ produces $p = 2.15 \pm 0.21$ ($\alpha = \frac{3p}{4}$) and the X-ray decline rate of $\alpha_{\rm X,late} = -2.10 \pm 0.15$ produces $p = 2.46 \pm 0.20$ ($\alpha = \frac{3p-1}{4}$; Ryan et al. 2020). The early and late-time behavior are consistent; thus throughout this work we assume an ISM-like density profile for GRB 160625B.[6]

There are significant features present in the early time radio data of GRB 160625B which are likely not related to the forward shock emission (Figure 2). A17 attribute these effects to the combination of a reverse shock and interstellar scintillation. Therefore when modeling the forward shock we conservatively choose to only include post-jet-break radio data ($\gtrsim$ 20 days) and at frequencies above 10 GHz (except for our late-time observation at 6.1 GHz) to mitigate these effects. A17 found there is negligible extinction due to dust within the GRB host galaxy and so we choose to ignore those effects in our analysis. Due to a systematic offset between the r- and i-band data of A17 and T17 we choose to only include that of T17 and none from A17 in our forward shock modeling as it is a larger dataset and observations were directly compared to the PanSTARRS magnitude system (see also K20).

3.2. *Afterglowpy Package*

[5] Strausbaugh et al. (2019) place the jet-break slightly earlier during the peak of the optical bump at ∼13 days

[6] A17, T17, K20 and other works come to the same conclusion.

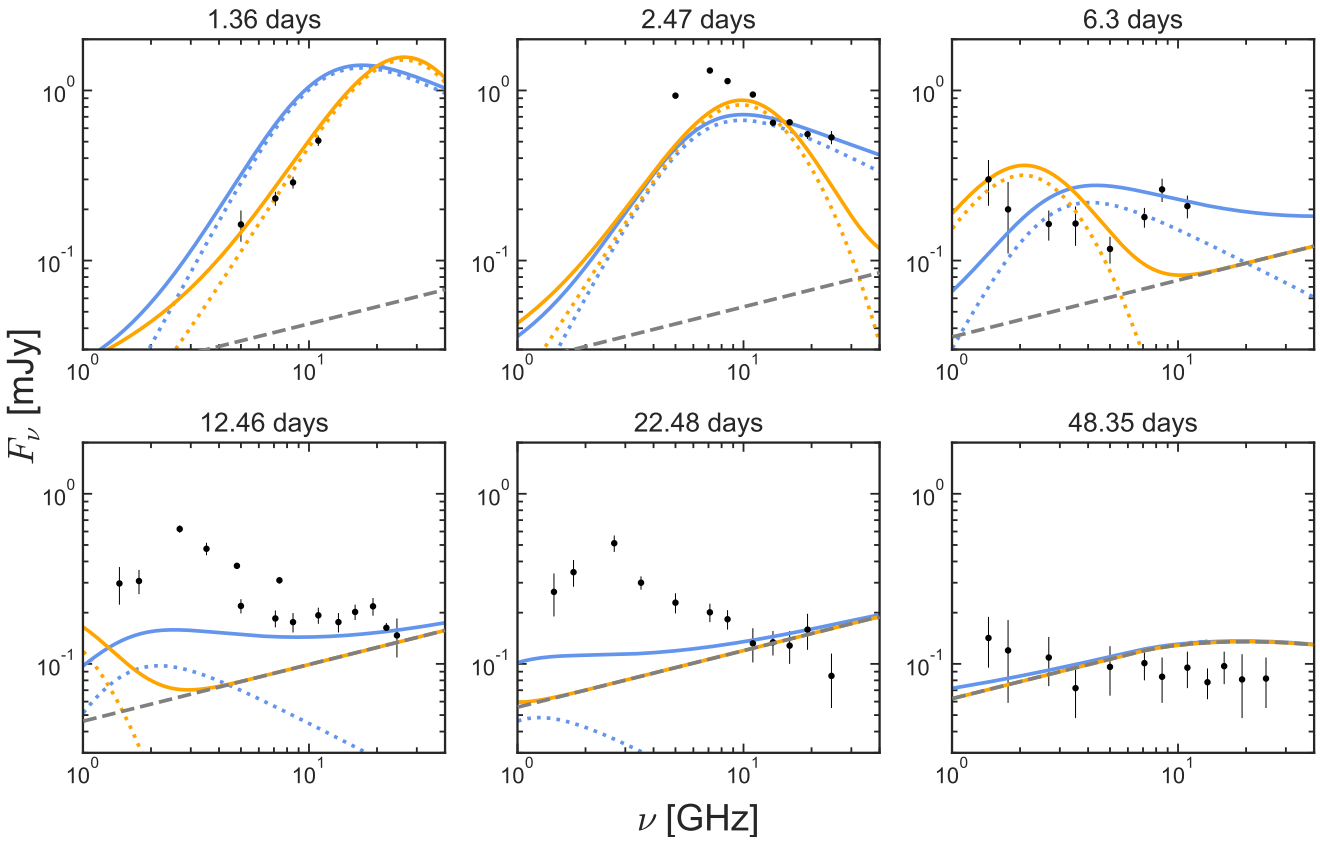


Figure 2. The observed spectral energy distributions (SEDs) for the radio data at various epochs overplotted with forward and reverse shock models. Our forward shock model (gray dashed line) is as described in §3.2.3. The two reverse shock models (dotted lines) are taken from A17 and represent different assumptions for the location of the SED peak, ν_p: $\nu_p = \nu_a$ (blue) and $\nu_p = \nu_c$ (orange). The solid lines represent the combination of both the forward and reverse shock models. Clearly the reverse shock, regardless of which model is used, dominates at early times (< 20 days) and lower frequencies (< 10 GHz).

`Afterglowpy` uses the single-shell approximation to numerically and analytically model a blast wave propagating through an ISM-like circumburst medium as a function of viewing angle and jet type (Ryan et al. 2020). A range of jet structure types have been proposed in the literature – some common examples include variations of top-hat, Gaussian, and power law models (Mészáros et al. 1998; Rossi et al. 2002; Zhang & Mészáros 2002; Rossi et al. 2004; Zhang et al. 2004; Aloy et al. 2005; Duffell & MacFadyen 2013a; Margutti et al. 2018; Coughlin & Begelman 2020). The exact structure of any one GRB jet may be dependent upon several factors such as the immediate circumburst environment and interactions with the stellar envelope. Compared to other available afterglow modeling codes (e.g., `BoxFit`; van Eerten et al. 2012) `afterglowpy` is advantageous for its ability to probe this complex inner structure of the GRB jet.

We employ the statistical sampling techniques of the EMCEE Python package for Markov-Chain Monte Carlo (MCMC; Foreman-Mackey et al. 2013) analysis with the `afterglowpy` models, as outlined in Troja et al. (2018). `Afterglowpy` generates samples from the entire posterior distribution for each of the models we consider here in this work. As input, our fit takes broadband fluxes, observation times, and instrument frequencies. As output, it produces samples from the posterior distribution for the viewing angle, θ_v, the isotropic kinetic energy released by the blastwave, $E_{\rm K,iso}$, jet core opening angle, θ_c, circumburst density, n, the spectral slope of the electron distribution, p, the fraction of shock energy imparted to electrons, ϵ_e, and to the magnetic field, ϵ_B.

For initial prior parameters we use the best fit parameters reported in K20. The assumed prior distributions and bounds for each parameter can be viewed in detail in Table 3 of Ryan et al. (2020). We assume a log-uniform prior distribution for $E_{\rm K,iso}$, n, ϵ_E, ϵ_B, and ξ and a uniform prior distribution for θ_c, θ_w, and p. The prior distribution for the viewing angle, θ_v, is constrained by the posterior probability distribution reported in Abbott et al. (2017).

3.2.1. *Top-Hat Jet Model*

We begin by first calculating the simplest model which could describe the outflow geometry, the top-hat. In this scenario, the energy of the jet is independent of angle and there is an instantaneous cutoff in energy at the jet edge:

$$E(\theta) = \begin{cases} E_0 & \theta \leq \theta_c \\ 0 & \theta > \theta_c \end{cases} \quad (1)$$

It is unlikely that a top-hat jet could be viewed far off-axis without a significant change in the appearance of the GRB afterglow (van Eerten et al. 2010; Zhang et al. 2015; Kathirgamaraju et al. 2016). Until recently, the top-hat model was assumed for most GRB analyses.

The covariances and posterior probability distributions of the various parameters are shown in Figure 3. Our best fit parameters for this model are listed in Table 4 and plotted in Figure 4. We allow the value of p to vary but restrict $\epsilon_e < 1/3$ and $\epsilon_B < 1/3$ (Alexander et al. 2017; Laskar et al. 2015). This is done primarily to remove degeneracies within the model fitting; however, we found that if we do not apply the restrictions on these microphysical parameters then the fits tend towards quite unphysical values (ϵ_B approaches 1.0). Therefore, we see this as further evidence that placing these restrictions is valid in this case. The parameters derived here imply a beaming-corrected kinetic energy of $E_K = E_{K,\rm iso}(1 - \cos\theta_c) = 1.2^{+0.2}_{-0.1} \times 10^{51}$ erg.

3.2.2. *Gaussian Jet Model*

To probe the jet structure we compare the simple top-hat to a more complex Gaussian model:

$$E(\theta) = \begin{cases} E_0\, e^{-\frac{\theta^2}{2\theta_c^2}} & \theta \leq \theta_w \\ 0 & \theta > \theta_w \end{cases} \quad (2)$$

where θ_w is the truncation angle of the Gaussian wings.

Similarly to the top-hat model we again restrict $\epsilon_e < 1/3$ and $\epsilon_B < 1/3$. In Gaussian models extended emission from the jet could be viewed at angles beyond θ_c and so larger values of θ_v are possible. The best fit parameters are listed in Table 4 and plotted in Figure 4. The covariances and posterior probability distributions of the parameters are shown in Figure 5.

To calculate the beaming-corrected energy we integrate Equation 2 over both jets:

$$E = 2\int_0^{\theta_w}\int_0^{2\pi} d\theta\, d\phi\, \sin\theta\, \frac{E(\theta)}{4\pi}, \quad (3)$$

which approximates to:

$$E \sim E_0\, \theta_c^2 \left(1 - e^{\frac{-\theta_w^2}{2\theta_c^2}}\right). \quad (4)$$

This gives a value for the beaming-corrected kinetic energy of $E_K = 8.4^{+1.2}_{-0.7} \times 10^{50}$ erg, which is slightly less than that found for the top-hat model.

3.2.3. *Gaussian Jet Model with Free ξ*

In the synchrotron afterglow model the emission is driven by a power-law distribution of electrons in the surrounding medium. The participation fraction, ξ, describes the percentage of total electrons which are accelerated by the passing shock wave and contribute to this power-law distribution. 100% participation ($\xi = 1$) is typically assumed in the literature but simulations have shown ξ can be as low as 10^{-2} (Sironi & Spitkovsky 2011; Sironi et al. 2013) and that lower values tend to be more realistic (Warren et al. 2018).

To test this we expand on our Gaussian model and now allow ξ to vary as a free parameter (Table 4). Notably, the beaming-corrected kinetic energy in this scenario is $E_K = 1.1^{+6.5}_{-0.9} \times 10^{53}$ erg, two orders of magnitude higher than in the previous cases. Such a high energy density may lead to concerns over the ability of the afterglow emission to avoid becoming suppressed by processes such as pair-production opacity. However, at the later times described here the afterglow has had sufficient time to expand and become diffuse. For an X-ray photon the opacity due to pair production is quite low ($\sim 10^{-8}$). This is because the number of high energy (GeV) photons with which the X-ray photon could pair-produce is small and so it is free to travel unhindered through the shock wave. During the prompt emission and possibly for GeV afterglows this could be a bigger concern, but for the later, more diffuse afterglow we do not consider it an issue.

We discuss this case in more detail in §4.3. The covariances and posterior probability distributions of the parameters are shown in Figure 6. We directly compare the previous top-hat and Gaussian jet models to this case in Figure 4 and plot the best fit over the data in Figure 7.

4. DISCUSSION

4.1. *Comparison to Past Works*

Previous works have completed similar analyses on GRB 160625B (T17, A17, K20). In each instance the jet is modeled with a conical top-hat structure and there is general agreement on the burst parameters (Table 4). We begin by simulating the light curves with `afterglowpy` using the model parameters found in A17, T17, and K20. We then compare the results to our own top hat solution in Figure 8.

K20 utilize the `BoxFit` package (van Eerten et al. 2012) to model the afterglow while A17 base their re-

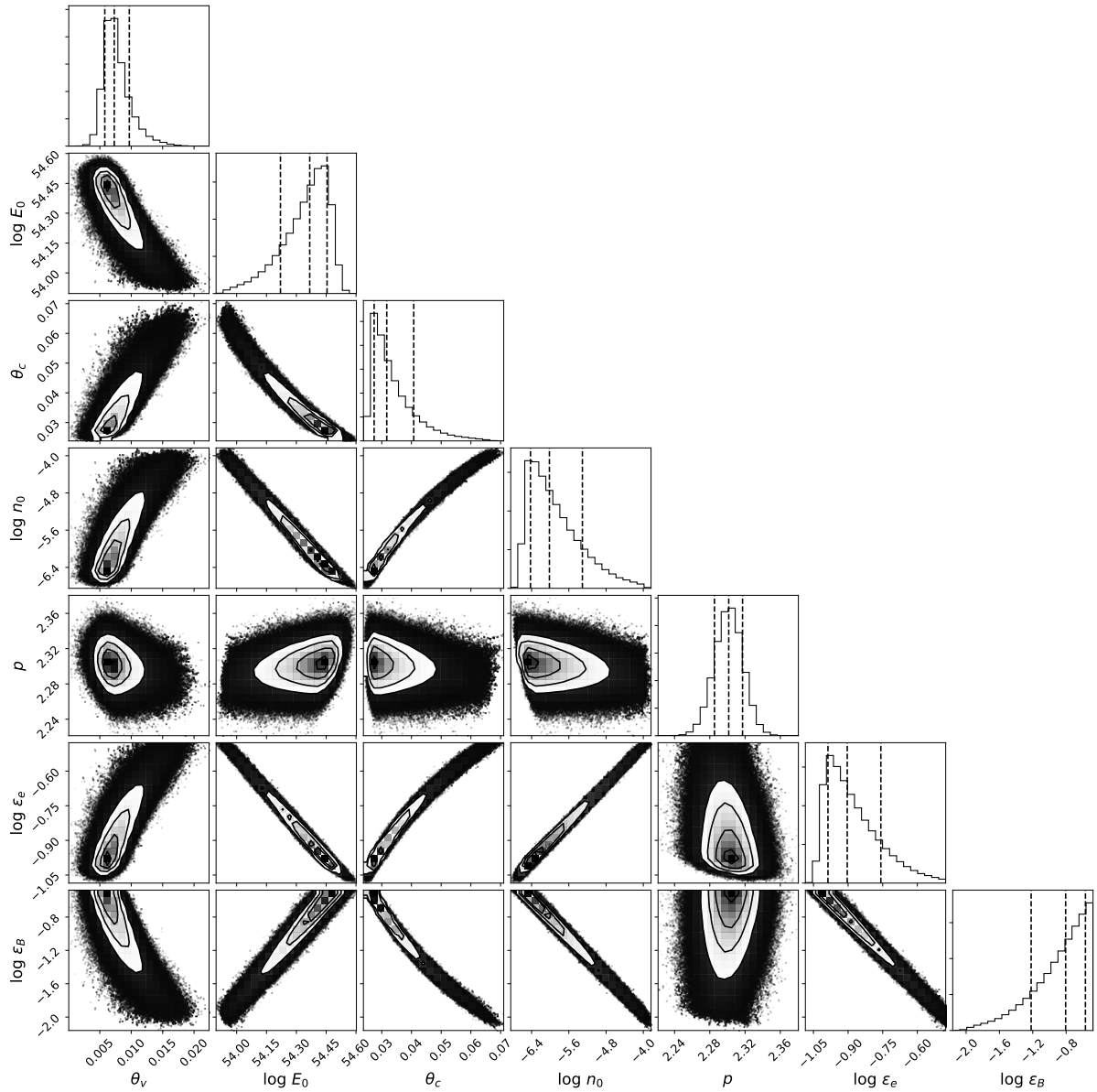


Figure 3. The covariances and posterior probability distributions of the parameters for the top-hat model (§3.2.1). The histograms denote the 15, 50, and 85 percentiles of the distributions.

sults on the synchrotron model described in Laskar et al. (2014, 2015). In Figure 8 the differences between the models at radio, optical, and X-ray wavelengths can be primarily explained by systematic offsets between `afterglowpy` and the other models used, differences in the datasets used, and the use of additional late-time data that was not available yet for A17 and T17. The largest discrepancies are seen at radio energies. This is partially due to the fewer number of observations available and the potential contamination of the forward shock by other radio effects. Recently Kangas & Fruchter (2019) have noted inconsistencies in observed jet break times between radio and higher frequencies; thus suggesting that radio afterglow light curves may simply not be well represented by standard afterglow theory. Jacovich et al. (2020) attribute this discrepancy to the lack of proper implementation of Klein-Nishina and effects in most afterglow modeling codes.

4.2. *Model Comparison with WAIC*

To quantify the differences between our own top-hat and Gaussian models described in §3.2 we utilize the Widely Applicable Information Criterion (WAIC; Watanabe 2010; Troja et al. 2020). The WAIC score provides an estimate of the expected log predictive density (elpd), i.e., how likely the model is to provide a good

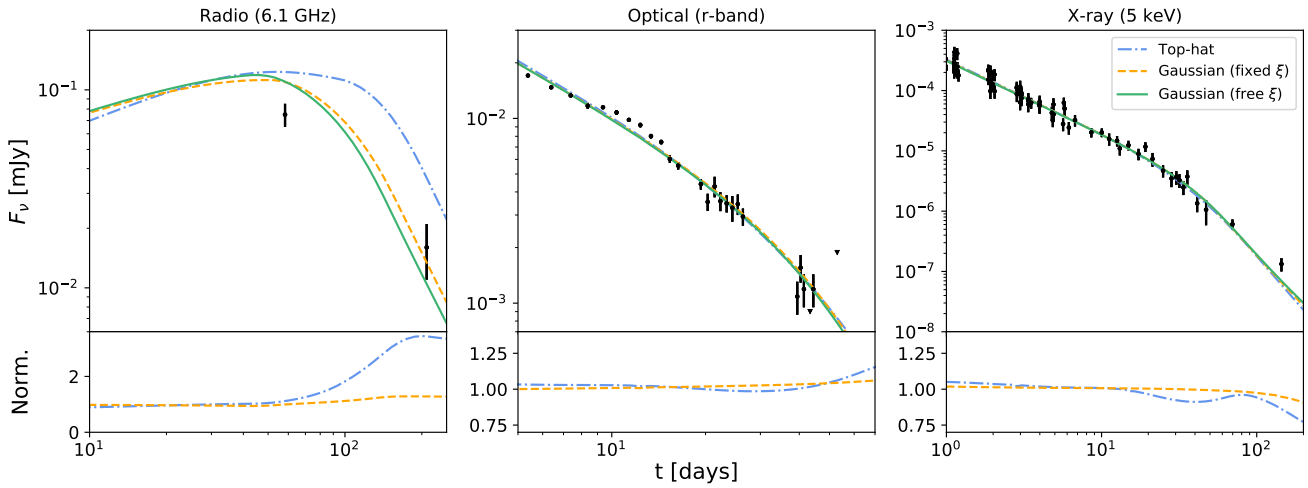


Figure 4. Top panel: Comparison between each of the three models described in §3.2: a top-hat jet (dash-dotted line), a Gaussian jet with ξ fixed to 1.0 (dashed line), and a Gaussian with ξ free to vary (solid line). Bottom panel: The top-hat and fixed-ξ Gaussian jet models are normalized by the free-ξ Gaussian jet model. The models provide comparable fits to the observed data except at later times in the radio.

fit for future data (Gelman et al. 2013). The elpd in general is quite hard to derive without prior knowledge of the true model but the WAIC score can be calculated directly from the MCMC statistical samples. In general, it is the difference between WAIC scores, rather than the raw WAIC score itself, which is most relevant. A model is considered strongly preferred, i.e., has greater predictive power, over another if the difference between their two WAIC scores is a factor of a few larger than the error on that difference. The uncertainty on the raw WAIC and WAIC difference scores is an estimate of the standard error and can be an underestimate but is usually accurate within a factor of 2 (Bengio & Grandvalet 2004). Therefore we list a significance range for the confidence level in Table 6.

As discussed in §3.2 we first began by directly comparing a top-hat and Gaussian style jet and then exploring the effects that varying the participation fraction, ξ, had on the GRB afterglow. Table 6 shows the model comparison between each of these three cases. Both Gaussian models show a greater predictive power compared to the simpler top-hat model but there is not a significant difference between the two Gaussian models themselves.

4.3. *The Participation Fraction, ξ*

In §3.2.3 we fit the afterglow of GRB 160625B with a Gaussian jet model but allowed the participation fraction, ξ, to vary. In agreement with the findings of Warren et al. (2018) our model prefers a lower value of $\xi \sim 0.01$, rather than total participation. Clearly, decreasing the participation fraction has dramatic effects on the other physical parameters. If all other parameters are kept fixed then the density of the circumburst environment must increase to provide the necessary number of electrons to produce the observed flux. This causes θ_c to increase as the relativistic jet interacts with more material. Increasing the density also results in a faster-evolving shock wave, so $E_{K,\rm iso}$ must increase to maintain the light curve shape. Most notably, ϵ_B decreases by four orders of magnitude due to the lack of accelerated electrons.

Figure 9 illustrates how varying ξ can have dramatic effects on the predicted afterglow light curve. We begin with the best fit parameter values of the top-hat jet and Gaussian (fixed-ξ) jet models from §3.2 but fix ξ to three different values – 1.0, 0.1, and 0.01 – and plot the results. We see the greatest differences at radio energies and at early times in the optical band. Those electrons which pass through the shock wave without being accelerated may increase the opacity to synchrotron self-absorption and also introduce an additional source of emission at very early times at optical wavelengths (∼few seconds post-burst) that then remains detectable at radio/millimeter wavelengths for several days or more (Ressler & Laskar 2017). Therefore, constraining the value of ξ is critical for understanding the implications of the total energy budget of the burst (§4.7) and the density of the local circumburst environment (§4.6).

4.4. *Sharp Edge Effects on p*

In both Gaussian jet fits the spectral slope of the electron distribution, p, is significantly lower than ∼2.3 which is the value found both analytically (§3.1) and in the top-hat model case (§3.2.1). When ξ is allowed to

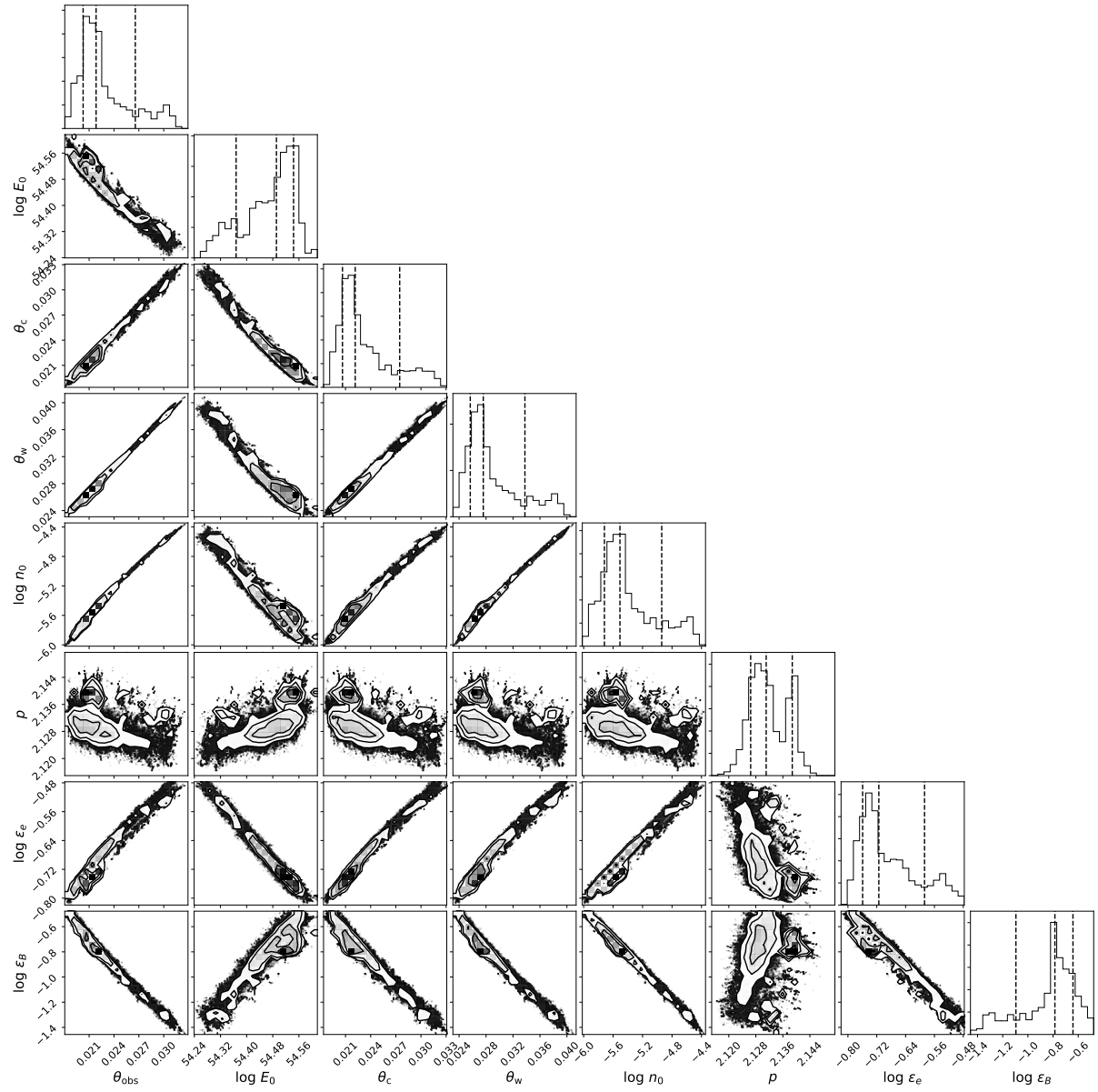


Figure 5. The covariances and posterior probability distributions of the parameters for the Gaussian model with ξ fixed to 1.0 (§3.2.2). The histograms denote the 15, 50, and 85 percentiles of the distributions.

vary p decreases from 2.13 ± 0.01 to 2.10 ± 0.01. This is explained by the favoured relationship between θ_c and θ_w. In both Gaussian models we find ${}^{\theta_c}/_{\theta_w} \sim 0.8$ meaning the emission does not extend greatly off-axis beyond the primary portion of the jet. Therefore, in slightly off-axis viewing angles the effect of a sharp edge may have a significant impact on the resulting light curve. Emission from one side of the jet reaches the viewer before the other side, resulting in slightly less observed flux than expected for a perfectly on-axis viewing angle. This manifests as a steepening of the light curve which can then allow p to instead probe lower values in the parameter distribution.

To investigate this we repeated the fit from 3.2.3 but now place a constraint where $\theta_w > 3\theta_c$ so as to force a 'softer' edge to the jet. In this scenario we find that p prefers a higher value of $2.23^{+0.02}_{-0.03}$, more consistent with the top-hat jet results, and $\theta_w = 0.59^{+0.32}_{-0.16}$ (Table 5). All other parameters remain consistent with those of the free-ξ case in Table 4. A softer-edged jet may represent a more physically realistic scenario compared to a sudden drop-off in emission at the jet edge. However, a WAIC analysis between this case (WAIC $= 799.0 \pm 126.8$) and

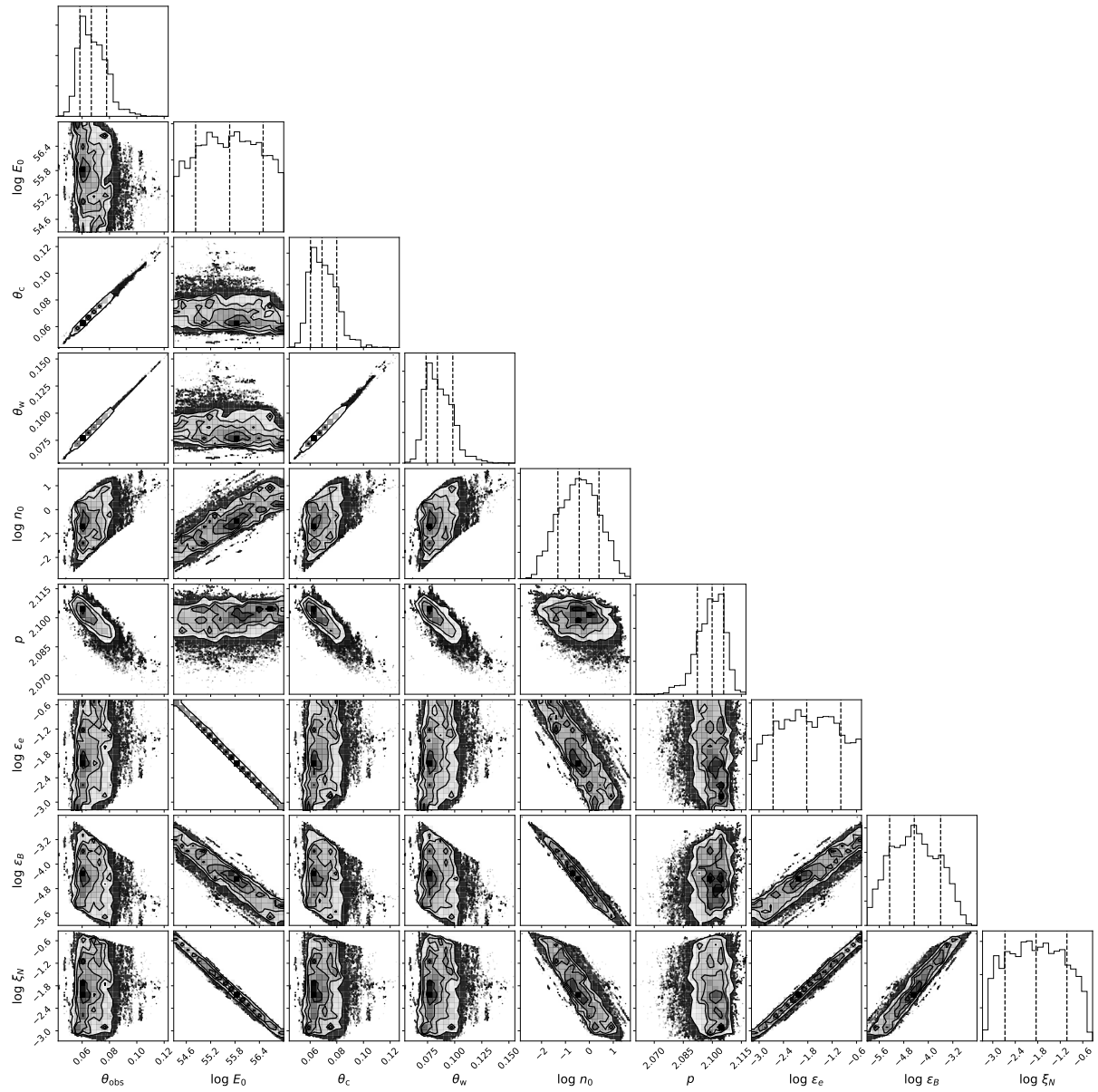


Figure 6. The covariances and posterior probability distributions of the parameters for the Gaussian model with ξ left to vary freely (§3.2.3). The histograms denote the 15, 50, and 85 percentiles of the distributions.

the freely varying ξ case (WAIC $= 1782.7 \pm 79.1$) shows better predictability for the sharp-edged case. This is, in fact, consistent with the results of Beniamini & Nakar (2019) where the authors claim that emission from structured jets cannot be observed far from the core of the jet.

4.5. *Viewing Angle Effects*

Precise predictions for GRB viewing angles have only become possible within the last few years thanks to the advent of various powerful high-resolution hydrodynamic simulations used both directly and indirectly by codes such as `BoxFit` (van Eerten et al. 2012), `ScaleFit` (Ryan et al. 2013), `JET` (Duffell & MacFadyen 2013b), and `afterglowpy` (Ryan et al. 2020). Ryan et al. (2015) show that, in fact, most GRBs are probably observed off-axis and the joint discovery of GW 170817/GRB 170817A highlighted just how significant viewing angle effects could be for a single event (Lazzati et al. 2018; Troja et al. 2018; Xie et al. 2018; Alexander et al. 2018; Wu & MacFadyen 2018; Fong et al. 2019; Troja et al. 2019; Lamb et al. 2020).

Underestimating the viewing angle of GRBs may introduce biases in the afterglow model fitting, e.g., by overestimating the beaming width of the jet (van Eerten

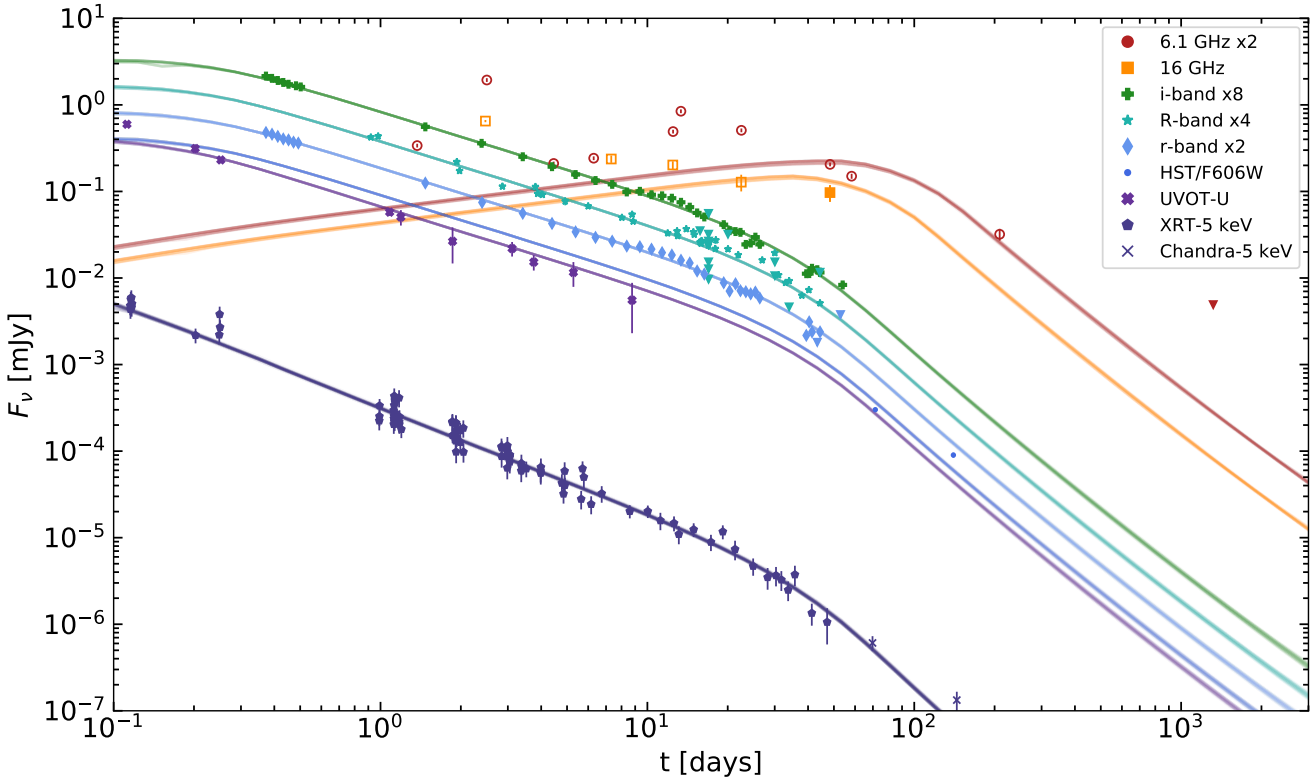


Figure 7. The multiwavelength light curve of GRB 160625B overplotted with our best fit model of the afterglow forward shock from §3.2.3: a Gaussian jet with ξ free to vary. Times are referenced from the GBM trigger (Jun 25 2016 22:40:16.28 UT). Open points represent radio data which were available but not included in the analysis (See §3.1 for more details). Transparent lines represent model uncertainties and are calculated via samples taken from the MCMC posterior distribution.

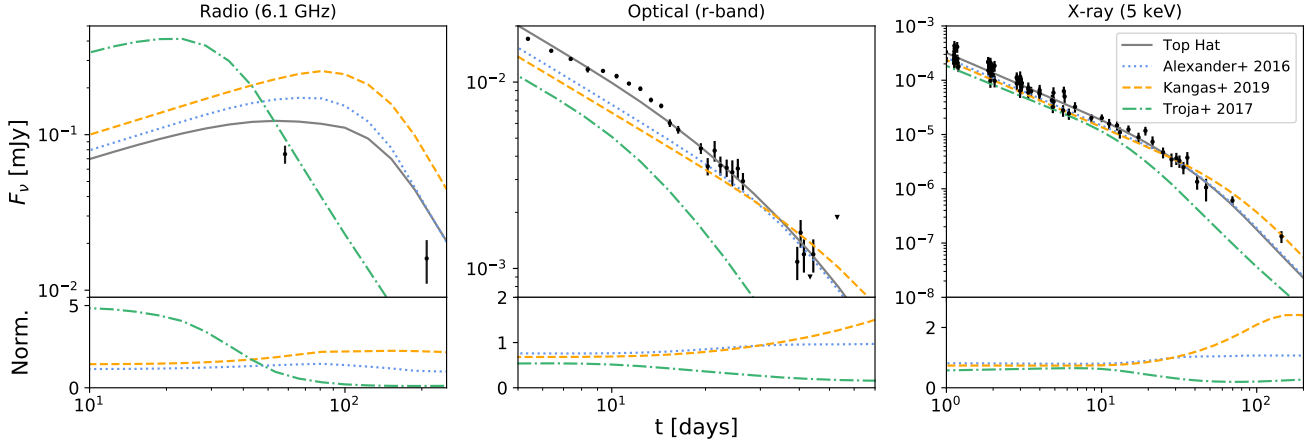


Figure 8. Top panel: Comparison between our top-hat jet model (solid line) to previous works from A17 (dotted line), K20 (dashed line), and T17 (dash-dotted line) (Table 4). Bottom panel: The A17, K20, and T17 models are normalized by our top hat model (§3.2.1). At X-ray wavelengths the models are almost indistinguishable at early times. The discrepancies between models are more apparent at radio and optical frequencies, where fewer observations are available.

2015). To illustrate this we repeat the Gaussian model with the same initial conditions as described in §3.2.2 but now we fix θ_v to an almost on-axis angle of 10^{-4} radians (Table 5). As a reference we note that *Swift* GRBs are thought to be observed more off-axis than this. Typical values of θ_v range from 0.055 to 0.42 radians (Ryan et al. 2015).

In this case we find that by assuming an on-axis viewing angle we are overestimating θ_c by a factor of ∼4.1 (compared to the fixed-ξ Gaussian jet model). Utilizing Equation 4 the beaming-corrected kinetic energy in this case is $E_K = 2.0^{+0.4}_{-0.1} \times 10^{51}$ erg. Although we have overestimated the beaming angle the slightly lower estimate for $E_{\rm K,iso}$ means the beaming-corrected kinetic energy remains consistent with the Gaussian case. Interestingly, the fact that ${}^{\theta_w}/_{\theta_c} < 1$ indicates a strong preference for a sharp jet edge as in the case of a top-hat jet. However, a WAIC comparison between this case (WAIC = 1145.7±197.1) and the Gaussian jet with fixed-ξ (WAIC = 1744.3±78.5) still shows better predictability and preference for a Gaussian-shaped jet model.

4.6. *Local Circumburst Environment*

Long GRBs are believed to result from the end state of massive stars (Woosley & Bloom 2006). Due to their short lifespan (tens of Myr), these massive stars live and die in the same dense molecular clouds which birthed them. It would appear to be a reasonable assumption to expect the local circumburst densities of GRBs to reflect that of regions of high star-formation (> 1 cm^{-3}). Observationally this is not usually the case, at least when assuming a top-hat jet model and ξ=1 (Laskar et al. 2015).

The derived value of the local circumburst density, n, for GRB 160625B is exceptionally low for most models in Table 4. This parameter can be difficult to constrain as it is highly degenerate with other physical parameters in the system. For most GRBs the value of n tends to be between $\sim 10^{-3}$ and $\sim 10^{2}$ cm^{-3} when assuming ξ=1 (Laskar et al. 2015). Density measurements between *Swift* and *Fermi* GRB populations tend to occupy discrete regions of parameter space, thus leading previous studies (e.g., Racusin et al. 2011) to suggest that these two populations may originate in different host environments, although there was not a large enough sample at the time to definitively confirm this.

The preference for ISM-like, low-density local environments may suggest LAT-detected long GRBs originate from lower-metallicity massive stars. This is motivated by the fact that these types of progenitor stars tend to have lower mass-loss rates (Kudritzki et al. 1987; Vink et al. 2001; Woosley et al. 2002). The ability for the relativistic jet to travel unhindered may also prevent the suppression of several radio components and can allow the reverse shock to propagate freely. GRB 160625B is one of only a few long-duration GRBs with a confirmed reverse shock (e.g., Laskar et al. 2013; Perley et al. 2014; Laskar et al. 2016, 2018, 2019).

In the standard afterglow model the circumburst density is intricately connected to other observed physical parameters. As noted in the case of the Gaussian jet with free-ξ (§3.2.3) our estimate of the local circumburst density is highly dependent upon the participation fraction. Decreasing ξ by a factor of 100 can increase n by upwards of five orders of magnitude. Therefore, further work on the impact of the participation fraction, ξ is required before a definitive association can be made between highly energetic long GRBs and massive, metal-poor progenitor stars.

4.7. *Energetics and Central Engine*

One of the main goals of this and future work will be calculating the beaming-corrected energy released by the GRB and especially how that relates to the physics of the central engine. Currently, two popular progenitor models are favored to explain the central engines of long GRBs: magnetars and black hole systems.

The spindown of a newborn millisecond pulsar could potentially power a long GRB via a Poynting-flux dominated relativistic outflow (Zhang & Mészáros 2001; Thompson et al. 2004). These magnetars are limited by their finite reserve of rotational energy. For a neutron star with a mass limit of $\sim 2\ M_\odot$, a radius of 10 km, and a spin period of about 1 ms places a cap on the available energy at $\sim 10^{52}$ erg (Metzger et al. 2007, 2011). This energy cap can be increased in the case of 'supramassive' neutron stars that have been stabilized by centrifugal forces and therefore could accommodate rotational energies of up to 10^{53} erg (Metzger et al. 2015). However, Beniamini et al. (2017) and Metzger et al. (2018) have recently shown that the true reservoir of available energy is unlikely to reach beyond $\sim few \times 10^{52}$ erg and so the magnetar model is in strong tension with at least the most energetic long GRBs.

In the second scenario, a black hole is formed in the immediate aftermath of the death of a massive star (Woosley 1993; MacFadyen & Woosley 1999; Woosley & Heger 2012). Stellar material accreting back onto the newly formed black hole may power relativistic jets. The jets burrow through the stellar envelope and provide an outlet for relativistic material to escape (Morsony et al. 2007). The typical 10-100 s durations of long GRBs correspond to the free-fall time of the star's

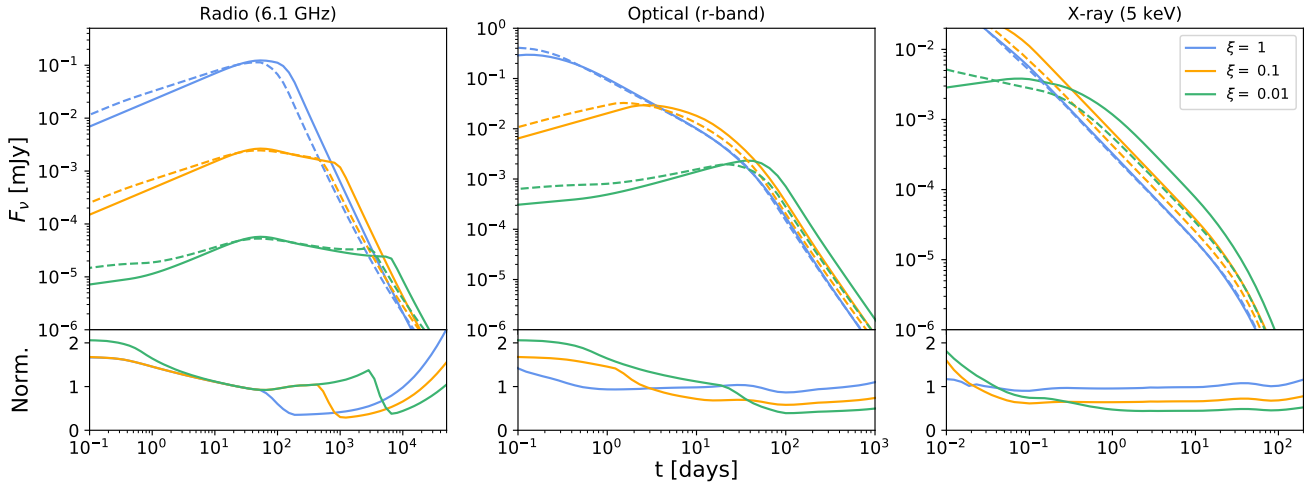


Figure 9. Top panel: We present the best fit parameter values of the top-hat (solid line) and Gaussian (dashed line) jet models from §3.2 but at three fixed values of ξ. The participation fraction, ξ, plays a pivotal role in the GRB afterglow, especially at radio energies. Lowering the value of ξ can have dramatic effects on the light curve. To account for the lower number of electrons contributing to the emission the total relativistic energy released must be increased and/or the density of the local circumburst environment must increase as well. Bottom panel: The Gaussian fluxes are normalized by the top-hat model for each value of ξ.

Table 4. Best Fit Model Parameters.

Model		This Work Top-Hat	This Work Gaussian (fixed ξ)	This Work Gaussian (free ξ)	A17 Top-Hat	K20 Top-Hat	T17 Top-Hat
θ_v	[rad]	$0.0073^{+0.0024}_{-0.0015}$	$0.022^{+0.006}_{-0.001}$	$0.066^{+0.010}_{-0.009}$	-	0.012	-
$E_{\rm K,iso}$	[erg]	$2.3^{+0.5}_{-0.7} \times 10^{54}$	$3.1^{+0.4}_{-0.8} \times 10^{54}$	$4.2^{+24}_{-3.5} \times 10^{55}$	$1.1^{+1.0}_{-0.5} \times 10^{54}$	1.8×10^{54}	$2.0^{+1.0}_{-1.4} \times 10^{54}$
θ_c	[rad]	$0.032^{+0.009}_{-0.004}$	$0.022^{+0.006}_{-0.001}$	$0.068^{+0.010}_{-0.010}$	0.063 ± 0.003	0.059	$0.042^{+0.028}_{-0.012}$
θ_w	[rad]	-	$0.028^{+0.007}_{-0.002}$	$0.083^{+0.014}_{-0.011}$	-	-	-
n	[cm^{-3}]	$9.6^{+39.0}_{-5.9} \times 10^{-7}$	$3.1^{+11}_{-1.1} \times 10^{-6}$	$0.352^{+1.71}_{-0.307}$	$(5 \pm 3) \times 10^{-5}$	1.1×10^{-5}	$1^{+49}_{-0.9} \times 10^{-4}$
p		2.30 ± 0.02	$2.13^{+0.01}_{-0.01}$	$2.10^{+0.01}_{-0.01}$	2.31 ± 0.01	2.30	2.2
ϵ_e		$0.12^{+0.05}_{-0.02}$	$0.19^{+0.07}_{-0.02}$	$0.017^{+0.085}_{-0.014}$	$0.23^{+0.07}_{-0.08}$	0.13	$0.10^{+0.22}_{-0.09}$
ϵ_B		$0.16^{+0.11}_{-0.10}$	$0.17^{+0.05}_{-0.09}$	$3.9^{+21.9}_{-3.3} \times 10^{-5}$	$0.013^{+0.11}_{-0.01}$	0.030	$0.010^{+0.090}_{-0.009}$
ξ		1.0	1.0	$0.016^{+0.080}_{-0.013}$	1.0	1.0	1.0
η [a]		$0.56^{+0.08}_{-0.05}$	$0.49^{+0.08}_{-0.03}$	$0.067^{+0.253}_{-0.057}$	$0.73^{+0.10}_{-0.14}$	0.62	$0.75^{+0.16}_{-0.09}$
$E_{\rm rel}$ [b]	[erg]	$2.7^{+1.3}_{-0.5} \times 10^{51}$	$1.6^{+0.6}_{-0.1} \times 10^{51}$	$1.2^{+6.5}_{-0.9} \times 10^{53}$	$2.3^{+1.8}_{-1.2} \times 10^{51}$	8.3×10^{51}	$\sim 6 \times 10^{51}$
$\chi^2/{\rm dof}$		1.24	0.99	0.86	1.26	8.6	-

Uncertainties are given at 1σ confidence levels. The reduced-χ^2 is the minimum over all completed runs.
[a] $\eta = \frac{E_{\gamma,\rm iso}}{E_{\gamma,\rm iso}+E_{\rm K,iso}}$, assuming $E_{\gamma,\rm iso} \sim 3 \times 10^{54}$ erg (Zhang et al. 2018)
[b] $E_{\rm rel} = E_\gamma + E_{\rm K}$

helium core. Unlike magnetars, these 'collapsars' have much less stringent caps on the potential energy which could be extracted. Theoretical predictions can easily produce energy releases greater than 10^{53} erg.

Previous estimates of the total relativistic energy ($E_{\rm rel} = E_\gamma + E_{\rm K}$) produced by GRB 160625B range from (2.3-8.3)$\times 10^{51}$ erg when assuming ξ=1 (Table 4). This is approaching but still within the upper limit of the magnetar model. We found in §3.2.2 that modeling the jet as a Gaussian rather than a top-hat leads to an estimate of the total relativistic energy that is below this range. Clearly, based on energetic arguments alone, we cannot rule out either the magnetar or collapsar model as progenitors. However, as noted in §3.2.3, assuming the participation fraction of electrons is unity is unlikely to be realistic. In agreement with K20, we find that more reasonable lower values of ξ produce an estimate of the total relativistic energy which is two orders of

magnitude higher (Figure 9). This value can still be reasonably accommodated by the collapsar model but is in strong tension with the energy cap expected from a magnetar. Regardless, it serves to show that without a better understanding of the participation fraction it will be difficult to draw robust conclusions regarding the progenitor.

5. CONCLUSIONS

With this work we have performed a case study of GRB 160625B to show the benefits of detailed multi-wavelength afterglow modeling as it pertains to understanding GRB energetics and environments. We modeled observations from radio to X-ray wavelengths spanning 0.1 to 1319 days post trigger. Using the standard afterglow framework we derived values for several physical parameters pertaining to the burst and performed a comparison between top-hat and Gaussian jet structure models. Our main conclusions can be summarized as follows:

- We fit GRB 160625B with a top-hat jet via the `afterglowpy` modeling package. We find general agreement in the afterglow parameters with previous top-hat jet models.
- Next, we fit the afterglow with a Gaussian-shaped jet. Although the derived density, kinetic energy, and other microphysical parameters remain consistent with the top-hat case we find that this jet shape is strongly preferred.
- Finally, we considered how allowing more freedom for the participation fraction, ξ, affects the afterglow parameters. This change had the most dramatic effect and resulted in a density which is 5 orders of magnitude higher, a value of ϵ_B which is 4 orders of magnitude lower, and a total relativistic energy which is 2 orders of magnitude higher. This has important implications for constraining the GRB local circumburst environment, central engine, and burst energetics.

Given that our models include several highly degenerate parameters it can be challenging to distinguish between their various subtleties. In Figure 10 we show how varying the viewing angle, θ_v, impacts the burst afterglow for both top-hat and Gaussian jet structures. There exists an offset in flux density at late times between the two models that is independent of waveband or viewing angle. Therefore the detection of GRBs viewed substantially off-axis ('orphan afterglows') may not be strictly necessary and future multi-wavelength observations at very late times could help further reinforce the preference for a Gaussian-shaped jet over a top-hat jet.

In future work we plan to continue our analysis on the afterglow modeling of bright LAT-detected long GRBs. These events typically have abundant data and also tend to be observed in low-density environments, thus providing an excellent sample for comparing jet structure models. We will use the results to expand on the arguments discussed here and create a comprehensive sample of well-documented LAT long GRBs and their general properties.

Analysis was performed on the YORP cluster administered by the Center for Theory and Computation, part of the Department of Astronomy at the University of Maryland. GR acknowledges the support from the University of Maryland through the Joint Space Science Institute Prize Postdoctoral Fellowship. A.C. acknowledges support from NSF CAREER award #1455090. A.H. acknowledges support by the I-Core Program of the Planning and Budgeting Committee and the Israel Science Foundation. The National Radio Astronomy Observatory is a facility of the National Science Foundation operated under cooperative agreement by Associated Universities, Inc. We acknowledge the use of public data from the Swift data archive.

Facilities: SWIFT (XRT, UVOT), CXO, HST, RATIR, LCOGT (FTN), Liverpool:2m, Magellan, Maidanak:1.5m, CrAO:1.25m, VLA, ATCA

REFERENCES

Abbott, B. P., Abbott, R., Abbott, T. D., et al. 2017, Nature, 551, 85, doi: 10.1038/nature24471

Ajello, M., Arimoto, M., Axelsson, M., et al. 2019, ApJ, 878, 52, doi: 10.3847/1538-4357/ab1d4e

Alexander, K. D., Laskar, T., Berger, E., et al. 2017, ApJ, 848, 69, doi: 10.3847/1538-4357/aa8a76

Alexander, K. D., Margutti, R., Blanchard, P. K., et al. 2018, ApJL, 863, L18, doi: 10.3847/2041-8213/aad637

Aloy, M. A., Janka, H. T., & Müller, E. 2005, A&A, 436, 273, doi: 10.1051/0004-6361:20041865

Amati, L., Frontera, F., & Guidorzi, C. 2009, A&A, 508, 173, doi: 10.1051/0004-6361/200912788

Table 5. Best Fit Gaussian Model Parameters for §4.4 and §4.5

		Soft Jet Edge	Fixed θ_v
θ_v	[rad]	$0.134^{+0.042}_{-0.039}$	10^{-4}
$E_{\rm K,iso}$	[erg]	$1.1^{+1.6}_{-0.7} \times 10^{55}$	$3.9^{+0.3}_{-0.6} \times 10^{54}$
θ_c	[rad]	$0.093^{+0.030}_{-0.026}$	0.09 ± 0.02
θ_w	[rad]	$0.59^{+0.32}_{-0.16}$	$0.024^{+0.003}_{-0.001}$
n	[cm^{-3}]	$4.1^{+25.2}_{-3.7}$	$3.4^{+4.6}_{-1.0} \times 10^{-7}$
p		$2.23^{+0.02}_{-0.03}$	$2.301^{+0.003}_{-0.005}$
ϵ_e		$0.076^{+0.113}_{-0.045}$	$0.079^{+0.015}_{-0.006}$
ϵ_B		$7.0^{+18}_{-4.0} \times 10^{-6}$	$0.25^{+0.06}_{-0.10}$
ξ		$0.061^{+0.054}_{-0.029}$	1.0
η [a]		$0.21^{+0.20}_{-0.11}$	$0.44^{+0.05}_{-0.02}$
$E_{\rm rel}$ [b]	[erg]	$1.3^{+0.9}_{-0.6} \times 10^{53}$	$2.0^{+0.4}_{-0.1} \times 10^{51}$
$\chi^2/{\rm dof}$		6.28	7.24

Uncertainties are given at 1σ confidence levels. The reduced-χ^2 is the minimum over all completed runs.
[a] $\eta = \frac{E_{\gamma,\rm iso}}{E_{\gamma,\rm iso}+E_{\rm K,iso}}$, assuming $E_{\gamma,\rm iso} \sim 3 \times 10^{54}$ erg (Zhang et al. 2018)
[b] $E_{\rm rel} = E_\gamma + E_{\rm K}$

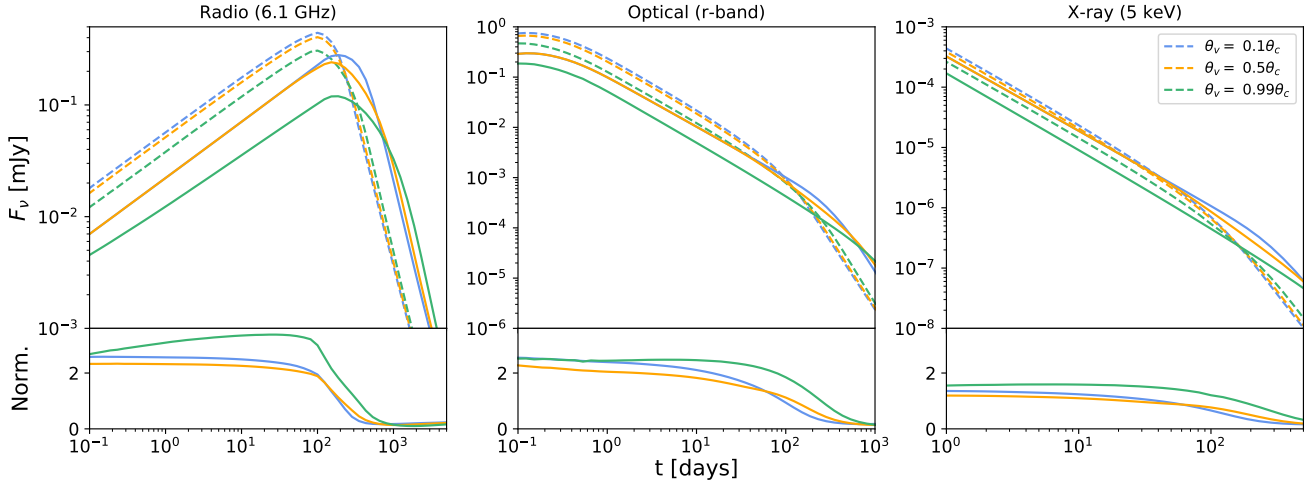


Figure 10. Top panel: Here we calculate the afterglow light curves for both a top-hat (solid line) and Gaussian (dashed line) jet structure at various points within the beam. We fix θ_c in the top-hat model so that $E_{\rm tot}$ remains the same in both models. All other parameters besides θ_v and θ_c are the same as listed in Table 4. Viewing a GRB off-axis has the greatest affect at early times as this is when edge effects are most noticeable. The differences between Gaussian and top-hat models are most apparent at later times. Bottom panel: The Gaussian fluxes are normalized by the top-hat models for each viewing angle.

Table 6. Model Comparison

	Gaussian (free ξ)	Gaussian (fixed ξ)	Top Hat
WAIC	1782.7 ± 79.1	1744.3 ± 78.5	-3561.8 ± 167.2
ΔWAIC/N	-	0.10 ± 0.09	-14.5 ± 2.7
Confidence Level	-	(0.58-1.16)σ	(2.7-5.3)σ

A WAIC analysis is performed for each model considered. A higher WAIC score indicates better predictability for future data based on the model. The Gaussian model with ξ free to vary has a higher likelihood of describing new data well so we use it as the base to compare the others. Each Gaussian model has a higher WAIC score compared to the top-hat case but there is no strong preference for the free-ξ over the fixed-ξ Gaussian model.

Atwood, W. B., Abdo, A. A., Ackermann, M., et al. 2009, ApJ, 697, 1071, doi: 10.1088/0004-637X/697/2/1071
Bengio, Y., & Grandvalet, Y. 2004, J. Mach. Learn. Res., 5, 1089–1105
Beniamini, P., Giannios, D., & Metzger, B. D. 2017, MNRAS, 472, 3058, doi: 10.1093/mnras/stx2095
Beniamini, P., & Nakar, E. 2019, MNRAS, 482, 5430, doi: 10.1093/mnras/sty3110
Berger, E., Kulkarni, S. R., & Frail, D. A. 2004, ApJ, 612, 966, doi: 10.1086/422809
Bloom, J. S., Frail, D. A., & Sari, R. 2001, AJ, 121, 2879, doi: 10.1086/321093
Burns, E. 2016, GRB Coordinates Network, 19587, 1
Burrows, D. N., Hill, J. E., Nousek, J. A., et al. 2005, SSRv, 120, 165, doi: 10.1007/s11214-005-5097-2
Cenko, S. B., Frail, D. A., Harrison, F. A., et al. 2010, ApJ, 711, 641, doi: 10.1088/0004-637X/711/2/641
—. 2011, ApJ, 732, 29, doi: 10.1088/0004-637X/732/1/29
Coughlin, E. R., & Begelman, M. C. 2020, MNRAS, doi: 10.1093/mnras/staa3026
Dirirsa, F., Vianello, G., Racusin, J., & Axelsson, M. 2016, GRB Coordinates Network, 19586, 1
Duffell, P. C., & MacFadyen, A. I. 2013a, ApJL, 776, L9, doi: 10.1088/2041-8205/776/1/L9
—. 2013b, ApJ, 775, 87, doi: 10.1088/0004-637X/775/2/87
Evans, P. A. 2016, GRB Coordinates Network, 19582, 1
Evans, P. A., Beardmore, A. P., Page, K. L., et al. 2007, A&A, 469, 379, doi: 10.1051/0004-6361:20077530
—. 2009, MNRAS, 397, 1177, doi: 10.1111/j.1365-2966.2009.14913.x
Fitzpatrick, E. L. 1999, PASP, 111, 63, doi: 10.1086/316293
Fong, W., Blanchard, P. K., Alexander, K. D., et al. 2019, ApJL, 883, L1, doi: 10.3847/2041-8213/ab3d9e
Foreman-Mackey, D., Hogg, D. W., Lang, D., & Goodman, J. 2013, PASP, 125, 306, doi: 10.1086/670067
Frail, D. A., Waxman, E., & Kulkarni, S. R. 2000, ApJ, 537, 191, doi: 10.1086/309024
Frail, D. A., Kulkarni, S. R., Sari, R., et al. 2001, ApJL, 562, L55, doi: 10.1086/338119
Gehrels, N., Chincarini, G., Giommi, P., et al. 2004, ApJ, 611, 1005, doi: 10.1086/422091
Gelman, A., Hwang, J., & Vehtari, A. 2013, arXiv e-prints, arXiv:1307.5928. https://arxiv.org/abs/1307.5928
Goldstein, A., Connaughton, V., Briggs, M. S., & Burns, E. 2016, ApJ, 818, 18, doi: 10.3847/0004-637X/818/1/18
Granot, J., & Sari, R. 2002, ApJ, 568, 820, doi: 10.1086/338966
Jacovich, T., Beniamini, P., & van der Horst, A. 2020, arXiv e-prints, arXiv:2007.04418. https://arxiv.org/abs/2007.04418
Kangas, T., & Fruchter, A. 2019, arXiv e-prints, arXiv:1911.01938. https://arxiv.org/abs/1911.01938
Kangas, T., Fruchter, A. S., Cenko, S. B., et al. 2020, ApJ, 894, 43, doi: 10.3847/1538-4357/ab8799
Kann, D. A. 2016, GRB Coordinates Network, 19579, 1
Kathirgamaraju, A., Barniol Duran, R., & Giannios, D. 2016, MNRAS, 461, 1568, doi: 10.1093/mnras/stw1441
Kocevski, D., & Butler, N. 2008, ApJ, 680, 531, doi: 10.1086/586693
Kudritzki, R. P., Pauldrach, A., & Puls, J. 1987, A&A, 173, 293
Lamb, G. P., Levan, A. J., & Tanvir, N. R. 2020, arXiv e-prints, arXiv:2005.12426. https://arxiv.org/abs/2005.12426
Laskar, T., Berger, E., Margutti, R., et al. 2015, ApJ, 814, 1, doi: 10.1088/0004-637X/814/1/1
Laskar, T., Berger, E., Zauderer, B. A., et al. 2013, ApJ, 776, 119, doi: 10.1088/0004-637X/776/2/119
Laskar, T., Berger, E., Tanvir, N., et al. 2014, ApJ, 781, 1, doi: 10.1088/0004-637X/781/1/1
Laskar, T., Alexander, K. D., Berger, E., et al. 2016, ApJ, 833, 88, doi: 10.3847/1538-4357/833/1/88
Laskar, T., Berger, E., Margutti, R., et al. 2018, ApJ, 859, 134, doi: 10.3847/1538-4357/aabfd8
Laskar, T., van Eerten, H., Schady, P., et al. 2019, ApJ, 884, 121, doi: 10.3847/1538-4357/ab40ce
Lazzati, D., Perna, R., Morsony, B. J., et al. 2018, PhRvL, 120, 241103, doi: 10.1103/PhysRevLett.120.241103
Lien, A., Sakamoto, T., Barthelmy, S. D., et al. 2016, ApJ, 829, 7, doi: 10.3847/0004-637X/829/1/7
MacFadyen, A. I., & Woosley, S. E. 1999, ApJ, 524, 262, doi: 10.1086/307790
Margutti, R., Alexander, K. D., Xie, X., et al. 2018, ApJL, 856, L18, doi: 10.3847/2041-8213/aab2ad
McMullin, J. P., Waters, B., Schiebel, D., Young, W., & Golap, K. 2007, in Astronomical Data Analysis Software and Systems XVI, ed. R. A. Shaw, F. Hill, & D. J. Bell, Vol. 376 (Astronomical Society of the Pacific Conference Series), 127
Meegan, C., Lichti, G., Bhat, P. N., et al. 2009, ApJ, 702, 791, doi: 10.1088/0004-637X/702/1/791
Mészáros, P., Rees, M. J., & Wijers, R. A. M. J. 1998, ApJ, 499, 301, doi: 10.1086/305635
Metzger, B. D., Beniamini, P., & Giannios, D. 2018, ApJ, 857, 95, doi: 10.3847/1538-4357/aab70c
Metzger, B. D., Giannios, D., Thompson, T. A., Bucciantini, N., & Quataert, E. 2011, MNRAS, 413, 2031, doi: 10.1111/j.1365-2966.2011.18280.x
Metzger, B. D., Margalit, B., Kasen, D., & Quataert, E. 2015, MNRAS, 454, 3311, doi: 10.1093/mnras/stv2224

Metzger, B. D., Thompson, T. A., & Quataert, E. 2007, ApJ, 659, 561, doi: 10.1086/512059

Morsony, B. J., Lazzati, D., & Begelman, M. C. 2007, ApJ, 665, 569, doi: 10.1086/519483

Nakahira, S., Yoshida, A., Sakamoto, T., et al. 2016, GRB Coordinates Network, 19617, 1

Panaitescu, A. 2007, MNRAS, 380, 374, doi: 10.1111/j.1365-2966.2007.12084.x

Perley, D. A., Cenko, S. B., Corsi, A., et al. 2014, ApJ, 781, 37, doi: 10.1088/0004-637X/781/1/37

Planck Collaboration, Aghanim, N., Akrami, Y., et al. 2018, arXiv e-prints, arXiv:1807.06209. https://arxiv.org/abs/1807.06209

Racusin, J. L., Liang, E. W., Burrows, D. N., et al. 2009, ApJ, 698, 43, doi: 10.1088/0004-637X/698/1/43

Racusin, J. L., Oates, S. R., Schady, P., et al. 2011, ApJ, 738, 138, doi: 10.1088/0004-637X/738/2/138

Ressler, S. M., & Laskar, T. 2017, ApJ, 845, 150, doi: 10.3847/1538-4357/aa8268

Rhoads, J. E. 1999, ApJ, 525, 737, doi: 10.1086/307907

Roming, P. W. A., Kennedy, T. E., Mason, K. O., et al. 2005, SSRv, 120, 95, doi: 10.1007/s11214-005-5095-4

Rossi, E., Lazzati, D., & Rees, M. J. 2002, MNRAS, 332, 945, doi: 10.1046/j.1365-8711.2002.05363.x

Rossi, E. M., Lazzati, D., Salmonson, J. D., & Ghisellini, G. 2004, MNRAS, 354, 86, doi: 10.1111/j.1365-2966.2004.08165.x

Ryan, G., Eerten, H. v., Piro, L., & Troja, E. 2020, ApJ, 896, 166, doi: 10.3847/1538-4357/ab93cf

Ryan, G., van Eerten, H., & MacFadyen, A. 2013, arXiv e-prints, arXiv:1307.6334. https://arxiv.org/abs/1307.6334

Ryan, G., van Eerten, H., MacFadyen, A., & Zhang, B.-B. 2015, ApJ, 799, 3, doi: 10.1088/0004-637X/799/1/3

Sari, R., Piran, T., & Halpern, J. P. 1999, ApJL, 519, L17, doi: 10.1086/312109

Sari, R., Piran, T., & Narayan, R. 1998, ApJL, 497, L17, doi: 10.1086/311269

Schlafly, E. F., & Finkbeiner, D. P. 2011, ApJ, 737, 103, doi: 10.1088/0004-637X/737/2/103

Sironi, L., & Spitkovsky, A. 2011, ApJ, 726, 75, doi: 10.1088/0004-637X/726/2/75

Sironi, L., Spitkovsky, A., & Arons, J. 2013, ApJ, 771, 54, doi: 10.1088/0004-637X/771/1/54

Strausbaugh, R., Butler, N., Lee, W. H., Troja, E., & Watson, A. M. 2019, ApJL, 873, L6, doi: 10.3847/2041-8213/ab07c0

Svinkin, D., Golenetskii, S., Aptekar, R., et al. 2016, GRB Coordinates Network, 19604, 1

Thompson, T. A., Chang, P., & Quataert, E. 2004, ApJ, 611, 380, doi: 10.1086/421969

Troja, E., Lipunov, V. M., Mundell, C. G., et al. 2017, Nature, 547, 425, doi: 10.1038/nature23289

Troja, E., Piro, L., Ryan, G., et al. 2018, MNRAS, 478, L18, doi: 10.1093/mnrasl/sly061

Troja, E., van Eerten, H., Ryan, G., et al. 2019, MNRAS, 489, 1919, doi: 10.1093/mnras/stz2248

Troja, E., van Eerten, H., Zhang, B., et al. 2020, arXiv e-prints, arXiv:2006.01150. https://arxiv.org/abs/2006.01150

van Eerten, H., van der Horst, A., & MacFadyen, A. 2012, ApJ, 749, 44, doi: 10.1088/0004-637X/749/1/44

van Eerten, H., Zhang, W., & MacFadyen, A. 2010, ApJ, 722, 235, doi: 10.1088/0004-637X/722/1/235

van Eerten, H. J. 2015, Journal of High Energy Astrophysics, 7, 23, doi: 10.1016/j.jheap.2015.04.004

Vink, J. S., de Koter, A., & Lamers, H. J. G. L. M. 2001, A&A, 369, 574, doi: 10.1051/0004-6361:20010127

von Kienlin, A., Meegan, C. A., Paciesas, W. S., et al. 2020, arXiv e-prints, arXiv:2002.11460. https://arxiv.org/abs/2002.11460

Warren, D. C., Barkov, M. V., Ito, H., Nagataki, S., & Laskar, T. 2018, MNRAS, 480, 4060, doi: 10.1093/mnras/sty2138

Watanabe, S. 2010, arXiv e-prints, arXiv:1004.2316. https://arxiv.org/abs/1004.2316

Willingale, R., Starling, R. L. C., Beardmore, A. P., Tanvir, N. R., & O'Brien, P. T. 2013, MNRAS, 431, 394, doi: 10.1093/mnras/stt175

Woosley, S. E. 1993, ApJ, 405, 273, doi: 10.1086/172359

Woosley, S. E., & Bloom, J. S. 2006, ARA&A, 44, 507, doi: 10.1146/annurev.astro.43.072103.150558

Woosley, S. E., & Heger, A. 2012, ApJ, 752, 32, doi: 10.1088/0004-637X/752/1/32

Woosley, S. E., Heger, A., & Weaver, T. A. 2002, Reviews of Modern Physics, 74, 1015, doi: 10.1103/RevModPhys.74.1015

Wu, Y., & MacFadyen, A. 2018, ApJ, 869, 55, doi: 10.3847/1538-4357/aae9de

Xie, X., Zrake, J., & MacFadyen, A. 2018, ApJ, 863, 58, doi: 10.3847/1538-4357/aacf9c

Xu, D., Malesani, D., Fynbo, J. P. U., et al. 2016, GRB Coordinates Network, 19600, 1

Xu, D., de Ugarte Postigo, A., Leloudas, G., et al. 2013, ApJ, 776, 98, doi: 10.1088/0004-637X/776/2/98

Yamazaki, R., Sato, Y., Sakamoto, T., & Serino, M. 2019, arXiv e-prints, arXiv:1910.04097. https://arxiv.org/abs/1910.04097

Zhang, B., Dai, X., Lloyd-Ronning, N. M., & Mészáros, P. 2004, ApJL, 601, L119, doi: 10.1086/382132

Zhang, B., & Mészáros, P. 2001, ApJ, 559, 110, doi: 10.1086/322400

—. 2002, ApJ, 571, 876, doi: 10.1086/339981

Zhang, B.-B., van Eerten, H., Burrows, D. N., et al. 2015, ApJ, 806, 15, doi: 10.1088/0004-637X/806/1/15

Zhang, B. B., Zhang, B., Castro-Tirado, A. J., et al. 2018, Nature Astronomy, 2, 69, doi: 10.1038/s41550-017-0309-8